

Giant and controllable Goos-Hänchen shift of a reflective beam off a hyperbolic metasurface of polar crystals

Tian Xue(薛天), Yu-Bo Li(李宇博), Hao-Yuan Song(宋浩元), Xiang-Guang Wang(王相光), Qiang Zhang(张强), Shu-Fang Fu(付淑芳), Sheng Zhou(周胜), and Xuan-Zhang Wang(王选章)
Citation: Chin. Phys. B, 2024, 33 (**1**): 014207. DOI: 10.1088/1674-1056/acdac2
Journal homepage: http://cpb.iphy.ac.cn; http://iopscience.iop.org/cpb

What follows is a list of articles you may be interested in

Nonlinear perturbation of a high-order exceptional point: Skin discrete breathers and the hierarchical power-law scaling

Hui Jiang(江慧), Enhong Cheng(成恩宏), Ziyu Zhou(周子榆), and Li-Jun Lang(郎利君)
Chin. Phys. B, 2023, 32 (**8**): 084203. DOI: 10.1088/1674-1056/accb47

High power, widely tunable femtosecond MgO:PPLN optical parametric oscillator

Jinfang Yang(杨金芳), Chong Wang(王翀), Weijun Ling(令维军), Jingwen Xue(薛婧雯), Xiaojuan Du(杜晓娟), Wenting Wang(王文婷), Yuxiang Zhao(赵玉祥), Feiping Lu(路飞平), Xiangbing Li(李向兵), Jiajun Song(宋贾俊), Zhaohua Wang(王兆华), and Zhiyi Wei(魏志义)
Chin. Phys. B, 2023, 32 (**7**): 074204. DOI: 10.1088/1674-1056/accd59

Two-photon absorption of $FAPbBr_3$ perovskite nanocrystals

Xuanyu Zhang(张轩宇), Shuyu Xiao(肖书宇), Xiongbin Wang(王雄彬), Tingchao He(贺廷超), and Rui Chen(陈锐)
Chin. Phys. B, 2023, 32 (**6**): 064212. DOI: 10.1088/1674-1056/acb203

Passively *Q*-switched diode-pumped Tm, Ho: $LuVO_4$ laser with a black phosphorus saturable absorber

Linjun Li(李林军), Tianxin Li(李天鑫), Long Zhou(周龙), Jianying Fan(范剑英), Yuqiang Yang(杨玉强), Wenqiang Xie(谢文强), Shasha Li(李莎莎)
Chin. Phys. B, 2019, 28 (**9**): 094205. DOI: 10.1088/1674-1056/ab33f1

Two-dimensional materials for ultrafast lasers

Fengqiu Wang(王枫秋)
Chin. Phys. B, 2017, 26 (**3**): 034202. DOI: 10.1088/1674-1056/26/3/034202

Giant and controllable Goos–Hänchen shift of a reflective beam off a hyperbolic metasurface of polar crystals

Tian Xue(薛天)[1], Yu-Bo Li(李宇博)[1], Hao-Yuan Song(宋浩元)[1], Xiang-Guang Wang(王相光)[1], Qiang Zhang(张强)[1], Shu-Fang Fu(付淑芳)[1,†], Sheng Zhou(周胜)[2,‡], and Xuan-Zhang Wang(王选章)[1]

[1] *Key Laboratory for Photonic and Electronic Bandgap Materials, Ministry of Education, and School of Physics and Electronic Engineering, Harbin Normal University, Harbin* 150025, *China*

[2] *Department of Basic Courses, Guangzhou Maritime University, Guangzhou* 510725, *China*

(Received 4 April 2023; revised manuscript received 30 May 2023; accepted manuscript online 2 June 2023)

We conduct a theoretical analysis of the massive and tunable Goos–Hänchen (GH) shift on a polar crystal covered with periodical black phosphorus (BP)-patches in the THz range. The surface plasmon phonon polaritons (SPPPs), which are coupled by the surface phonon polaritons (SPhPs) and surface plasmon polaritons (SPPs), can greatly increase GH shifts. Based on the in-plane anisotropy of BP, two typical metasurface models are designed and investigated. An enormous GH shift of about $-7565.58\lambda_0$ is achieved by adjusting the physical parameters of the BP-patches. In the designed metasurface structure, the maximum sensitivity accompanying large GH shifts can reach about 6.43×10^8 λ_0/RIU, which is extremely sensitive to the size, carrier density, and layer number of BP. Compared with a traditional surface plasmon resonance sensor, the sensitivity is increased by at least two orders of magnitude. We believe that investigating metasurface-based SPPPs sensors could lead to high-sensitivity biochemical detection applications.

Keywords: Goos–Hänchen shift, black phosphorus, surface plasmon phonon polaritons, sensitivity, metasurfaces

PACS: 42.65.–k, 81.05.Xj, 77.22.Ch, 07.07.Df **DOI:** 10.1088/1674-1056/acdac2

1. Introduction

Real light beams with finite lateral width reflected at dielectric surfaces appear to be shifted in-plane and out-of-plane, which is not entirely consistent with geometrical optics predictions. The Goos–Hänchen (GH) shift[1] refers to the beam shift parallel to the plane of incidence, while the Imbert–Fedorov (IF) shift[2] refers to the beam shift perpendicular to the incident plane. Artmann first theoretically described the GH shift in the regime of classical physics in 1948.[3] Optical losses due to optical absorption or scattering cannot be ignored in most materials, particularly metals. As a result, at an ordinary dielectric interface, the GH shift will be the same as the incident wavelength. The development of weak measurement technology has expanded the GH shift's potential applications,[4] including the accurate measurement of optical properties.[5] Several studies have been conducted on various dielectric surfaces to enhance the GH shift, such as the metasurfaces,[6] topological insulators,[7] Weyl semimetals,[8] and metamaterials (MMs),[9,10] as well as two-dimensional (2D) atomic crystals,[11] and so on. A structure known as subwavelength gratings was recently used to improve the GH shift.[12] Wu *et al.*, for example, demonstrated massive GH shifts in a compound grating waveguide structure that is aided by bound states in the continuum (BICs).[13,14]

Due to their special electronic and optical properties, 2D atomic crystals have revealed a variety of physical phenomena since the discovery of graphene.[15] The hyperbolic properties of graphene-based MMs can be achieved by adjusting the chemical potential controlled by the gate voltage or the doping level.[16] As an alternative to graphene, black phosphorus (BP) has received more attention, showing extraordinary potential in many applications, including photodetectors,[17] phase shifters,[18] and absorbers.[19] Unlike graphene, BP processes the puckered honeycomb lattice structure, resulting in the significant in-plane anisotropy. Furthermore, BP has a direct and layer-sensitive bandgap ranging from 0.3 eV to 2 eV, making it a remarkable material capable of achieving a tunable optical response over a broad range of wavelengths.[20] It is worth noting that 2D BP monolayers have been used in the development of polarization-sensitive broadband photodetectors, as well as traditional terahertz (THz) absorbers.[21] Motivated by the emergence of stacked 2D materials with a twist angle, the spatial shifts of the reflective beam from the hBN covered by a rotated BP layer are investigated.[22] Reference [23] investigated the spin Hall effect (SHE) on the surface of a twisted few-layer BP film, and discovered that an in-plane shift occurs and is sensitive to the twist angle. Surface plasmon polaritons (SPPs) can also be generated on the surface of a 2D BP film, which makes it a viable option for designing optoelectronic devices.[24]

Ionic crystals (ICs), which constitute the majority of polar crystals, possess at least one reststrahlen band (RB) where the

†Corresponding author. E-mail: shufangfu1975@163.com

‡Corresponding author. E-mail: zhousheng_wl@126.com

© 2024 Chinese Physical Society and IOP Publishing Ltd

longitudinal and transverse components of permittivity have the opposite sign.[25] The optical phonon mode of lattice vibration in ICs strongly couples with electromagnetic waves to form surface phonon polaritons (SPhPs) in the THz range. Unlike photonic crystals and metamaterials, the excited SPhPs on the surface of ICs can travel longer distances than SPPs due to the much lower optical losses of ICs.[26] In the infrared to THz range, SPhPs can support sub-diffraction limited near-field imaging, extraordinary transmission, and so on.[27]

For conventional types of sensors that typically use noble metal like gold or silver to improve sensor sensitivity,[28] it is still a challenging to improve sensor sensitivity due to the low binding ability of gold with biomolecules and the poor chemical stability of silver in the air. Monitoring GH shift signals by controlling the structural parameters and material characteristics is an efficient way to realize the sensing performance. Based on this concept, a sensor that works in the THz range by measuring the GH shift effect is promised. A new dissolved oxygen sensor based on surface plasmon resonance (SPR) and GH shift has been proposed, where the hemoglobin is immobilized on the sensor chip through self-assembled monolayers.[29] A highly sensitive short-range mode resonance sensor made of multilayer structured hyperbolic MMs with a maximum sensitivity of 330 μm/RIU in the near-infrared band has recently been designed.[30] Reference [31] describes a graphene–MoS_2 heterostructure-coated Au GH shift sensor with a sensitivity of 5.545×10^5 λ_0/RIU. The sensibility of a bimetallic sensor based on graphene–hBN heterostructure can be improved by enhancing the GH shift in the infrared band, and a sensibility of 202×10^5 λ_0/RIU can be achieved.[32] By precisely controlling the GH shift in the graphene–substrate system at the optical communication band, Zhou *et al*. created a refractive index sensor with adjustable sensitivity coefficient, which can be increased to $\pm1\times10^8$ λ_0/RIU by adjusting the Fermi energy.[33] In this work, we propose a metasurface structure made of polar crystals with BP-patches. The properties of the metasurface can be altered by adjusting parameters of BP-patches, such as in-plane anisotropy, size, carrier density, and layer number. Another important feature is that the surface plasmon phonon polaritons (SPPPs) will be excited at the interface between the BP-patches and the polar crystal, which is coupled by SPPs in BP and SPhPs in the polar crystal. It has been proven that the generation of SPPPs is beneficial to enhance the spatial shift.[34,35] Based on these advantages, the proposed novel sensing method based on the enhanced GH shift exhibits superior sensibility, namely, the maximum sensitivity is up to 6.43×10^8 λ_0/RIU, which is almost two orders of magnitude higher than the conventional sensor. We believe that this work is conducive to the design of GH shift sensors in THz range, and may also play an important role in highly sensitive detection.

This paper is organized as follows. Section 2 describes the metasurface structure created by the BP-patches, ZnS crystal, and sensor medium. Using the transfer matrix and equivalent circuit models, we provide a theoretical analysis of the GH shift and the proposed sensor device. Section 3 discusses how numerical simulations are used to verify the accuracy of theoretical models and provide additional physical insights. Finally, we summarize our findings in Section 4.

2. Theoretical model and method

In Fig. 1(a), a hyperbolic metasurface based on BP-patches is constructed. The thickness of IC is d and the period of BP-patches is set to D along the x- and y-axes. A sensing layer (SL) under the IC is utilized to detect the slight changes in its refractive index based on the GH shift. L_x and L_y indicate the lengths of the BP-patch along the x- and y-directions, respectively. The case where the armchair (AC) and the zigzag (ZZ) along the x- and y-directions is referred to as the model-I. The model-II is defined when the directions of the armchair and zigzag are switched, as shown in Fig. 1(b). The corresponding equivalent circuit model is plotted in Fig. 1(c). We assume that a radiation beam impinges on the hyperbolic metasurface with incident angle θ. With the help of Kubo's formula, the Drude model of BP conductivity can be described by[36]

$$\sigma_j=\frac{\mathrm{i}e^2}{\omega+\mathrm{i}\eta}\frac{n_\mathrm{B}}{m_j}+s_j\frac{e^2}{4\hbar}\left[\Theta(\omega-\omega_j)+\frac{\mathrm{i}}{\pi}\ln\left|\frac{\omega-\omega_j}{\omega+\omega_j}\right|\right],\quad(j=x,y),\tag{1}$$

where n_B is the carrier density, η, m_j, and s_j represent the relaxation time, the effective mass of electrons, and the different strengths of the interband component along the j direction, respectively. ω_j is the frequency of the interband transitions for the j component. Θ is the step function. It is worth noting that the optical conductivity of an ultrathin BP film containing several monolayers ($N<6$) can be approximated as $N\sigma_j$,[37] where N represents the layer number of BP film. The dielectric constant of the IC as the function of frequency is normally expressed as[38]

$$\varepsilon_\mathrm{d}=\varepsilon_\mathrm{h}+\frac{(\varepsilon_\mathrm{l}-\varepsilon_\mathrm{h})f_\mathrm{T}^2}{f_\mathrm{T}^2-f^2-\mathrm{i}f\tau_\mathrm{d}},\tag{2}$$

where ε_h and ε_l are the high and low frequency permittivity, f_T is the transverse lattice vibration frequency, and τ_d represents the damping of optical loss. The RB of IC is shown by $1<f/f_\mathrm{T}<\sqrt{\varepsilon_\mathrm{l}/\varepsilon_\mathrm{h}}$ if the damping responsible for losses is ignored. The dielectric constant of the SL can be

$$\varepsilon_\mathrm{SL}=(1.8+\Delta n)^2,\tag{3}$$

where Δn refers to the change of refractive index of sensing medium.[31] Since the dimension of the unit-cell is assumed

to be subwavelength, the surface with the patch-array can be characterized by a homogeneous surface impedance. For TM-waves, the surface impedance of BP-patches can be expressed by[39]

$$Z_{\rm BP}(\omega) = R + {\rm i}(\omega L - \frac{1}{\omega C}) = \frac{D}{L_y \sigma_x} - {\rm i}\frac{\eta_{\rm eff}}{2\alpha_x}\frac{L_x}{L_y}, \tag{4}$$

where $\eta_{\rm eff} = \sqrt{\mu_0/(\varepsilon_0 \varepsilon_{\rm eff})}$ is the wave impedance of the uniform host medium. $\varepsilon_{\rm eff}$ indicates the effective permittivity of the space surrounding the BP-patches. If the medium above and below the BP-patches is air and IC, then the effective permittivity can be expressed as $\varepsilon_{\rm eff} = (1+\varepsilon_{\rm d})/2$ as if the BP-patches are immersed in an equivalent effective medium.[40] α_x is the grid parameter along the x-axis and can be expressed by $\alpha_x = \frac{Dk_{\rm eff}}{\pi}\ln(\csc\frac{\pi L_x}{2D})$. $k_{\rm eff} = \omega\sqrt{\varepsilon_0\mu_0\varepsilon_{\rm eff}}$ is the wave number of the incident wave in the effective host medium. μ_0, ε_0, and k_0 are the permeability, permittivity, and the wave number in free space, respectively. The impedance represented in Eq. (4) is considered as a series R–L–C circuit, where the first impedance corresponds to the series R–L given by the product of the surface impedance and the geometric factor D/L_y. The second term of the impedance corresponds to a capacitive impedance associated with the BP-patch geometry and background environment. The characteristic impedance of the IC or SL for TM-waves is determined by

$$Z_j(\omega) = \frac{\eta_0}{\varepsilon_j}\sqrt{\varepsilon_j - \sin^2\theta}, \quad (j = \text{IC or SL}). \tag{5}$$

A serial relationship exists between the IC layer and the semi-infinite SL, and the serial impedance is

$$Z_{\rm ZS} = Z_{\rm IC}\frac{Z_{\rm SL} + {\rm i}Z_{\rm IC}\tan(d_{\rm IC}\sqrt{k_{\rm IC}^2 - k_{\rm SL}^2})}{Z_{\rm IC} + {\rm i}Z_{\rm SL}\tan(d_{\rm IC}\sqrt{k_{\rm IC}^2 - k_{\rm SL}^2})}, \tag{6}$$

where $k_j = \omega\sqrt{\mu_0\varepsilon_0\varepsilon_j}$ is the wave number of the incident wave. Based on the above discussion, the hyperbolic metasurface impedance of the proposed ZnS–BP–SL structure is calculated by[41]

$$Z_{\rm tot}(\omega) = Z_{\rm BP}(\omega) \parallel Z_{\rm ZS}(\omega), \tag{7}$$

and the symbol "$\parallel$" represents the parallel relationship between $Z_{\rm BP}$ and $Z_{\rm zs}$. The reflective coefficient is expressed by

$$r = \frac{Z_{\rm tot}(\omega) - Z_0}{Z_{\rm tot}(\omega) + Z_0}, \tag{8}$$

here the free space impedance for different incident angles is given as $Z_0 = \eta_0\cos\theta$, where $\eta_0 = 120\pi$ is the plane wave impedance in free space. The GH shift is then obtained by the well-known result[42]

$$\Delta x = -\frac{\lambda_0}{2\pi}{\rm Im}(\frac{1}{r}\frac{\partial r}{\partial\theta}), \tag{9}$$

where λ_0 is the vacuum wavelength of the incident light. Obviously, the GH shift can reach a peak when the phase difference experiences a sharp variation with the incident angle. Finally, the phase (ϕ) and reflectivity (R) of reflection coefficient are obtained from the formulae

$$\phi = \arg(r), \quad R = |r|^2. \tag{10}$$

We define ΔGH as the change of GH shift with the changing of the refractive index and $\Delta n = 0.0002$. Therefore, the sensitivity can be defined as[32]

$$S = \frac{\Delta GH}{\Delta n}. \tag{11}$$

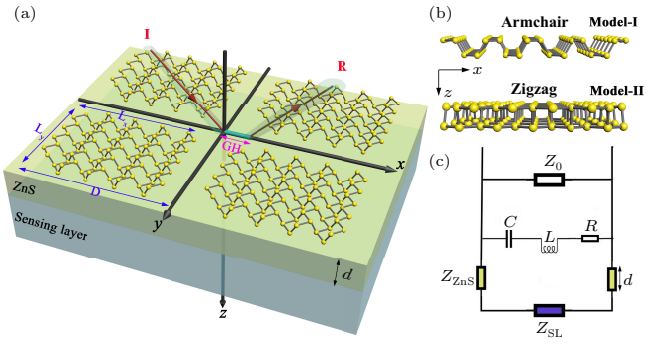


Fig. 1. (a) Schematic diagram of the spatial shift on the metasurface of BP–ZnS–SL. (b) Model-I is defined as the armchair (AM) direction along the x-axis and model-II means the zigzag (ZZ) along x-axis. (c) The equivalent circuit diagram of this structure.

3. Results and discussion

For subsequent theoretical and numerical calculations, both the BP-patch period (D) and the thickness of ZnS (d) are 500 nm, and L_x and L_y are fixed at 100 nm. Of course, the structure parameters of BP can be adjusted to flexibly control the GH shift. The ZnS crystal is selected as an example where $f_{\rm T} = 8.22$ THz, $\varepsilon_{\rm h} = 5.0$ and $\varepsilon_{\rm l} = 8.3$.[43] The damping of ZnS is supposed to be $\tau_{\rm d} = 3\ {\rm cm}^{-1}$. Figure 2 presents the permittivity of ZnS versus the frequency. In the region of $f_{\rm T} < f < 1.2884 f_{\rm T}$ situated in the mid-infrared range, the ZnS crystal possesses a negative permittivity which leads to the hyperbolic properties. For the conductivity of BP, a particular set of parameters for model-I is used, namely, $m_x = 0.2m_0$ and $m_y = 0.7m_0$ (m_0 is the static electron mass), $\eta = 0.01$ eV $\omega_x = 1.0$ eV, $s_x = 1.7$, $\omega_y = 0.35$ eV, and $s_y = 3.7$.[44] For model-II, we only need to exchange the electron mass along x- and y-directions. The real and imaginary parts of BP conductivity as a function of the frequency under the different $n_{\rm B}$ are illustrated in Fig. 3. At $f = 38.48$ THz, a transition takes place for the real part of $\sigma_{\rm AC}$ and a dip is observed for the imaginary part. It is well-known that the BP exhibits the strong structure anisotropy, which means that the puckered lattice results in two inequivalent directions in-plane. As a result, the transition point for the real part of $\sigma_{\rm ZZ}$ occurs at about 13.74 THz,

which is close to the RB of ZnS. In addition, the values of conductivity increase with the increasing n_B. The electromagnetic response of the anisotropic 2D material is normally classified into two district regions. In the lower frequency region, the conductivity is considered as a pure Drude type, where the in-plane anisotropy results from the effective mass of the electrons traveling in various directions. Yet, the contribution from interband electron transitions may become dominant at higher frequencies. In the following discussions, we mainly focus on the two typical models.

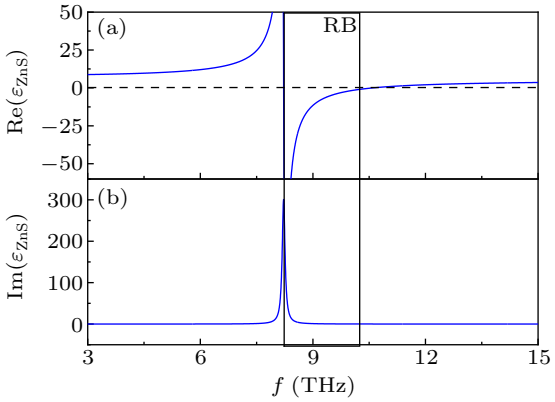


Fig. 2. (a) Real and (b) imaginary parts of permittivity of ZnS slab versus frequency. The colored region indicates the RB.

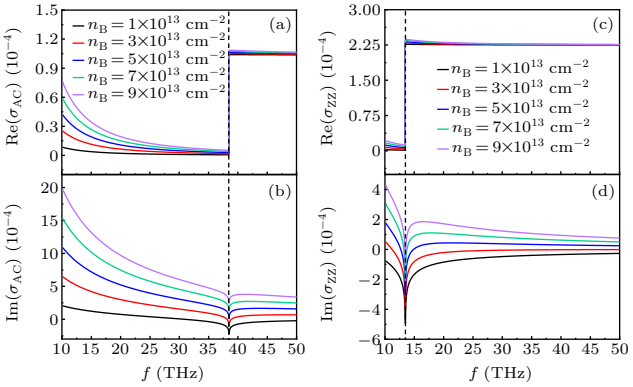


Fig. 3. Conductivity of BP as a function of the frequency under the different n_B and the transition occurs at (a) $f = 38.48$ THz for σ_{AC} and (b) $f = 13.48$ THz for σ_{ZZ}.

The relative impedance and the GH shift versus the frequency at $N = 1$ and $n_B = 1.0 \times 10^{13}$ cm^{-2} are presented in Fig. 4. For model-I shown in Fig. 4(a), the relative impedance amplitude undergoes two transitions located in the lower and higher frequency regions, respectively. The first transition occurs at 11.2 THz, which is just close to the right boundary of the ZnS's RB (see Fig. 2). The other transition near 38.48 THz should be caused by the BP layer if we check its conductivity. An obvious GH shift is observed near the first transition at $f = 11.12$ THz where the impedance approaches to zero, as shown in Fig. 4(b). As a result of the zero reflection (see Eq. (8)), the incident angle will be close to the Brewster angle. When the BP's zigzag direction is rotated to the direction of the armchair, only a transition in the lower frequency region is preserved and shifts from the higher frequency to the lower frequency, as illustrated in Fig. 4(c). The inset in Fig. 4(c) also indicates that the significant GH shift normally is excited near Brewster angles, as shown in Fig. 4(d). It is reasonable to predict that the impedance transition is the result of the joint action of BP and ZnS. The in-plane anisotropy of BP will play a crucial role in the generation of large GH shifts.

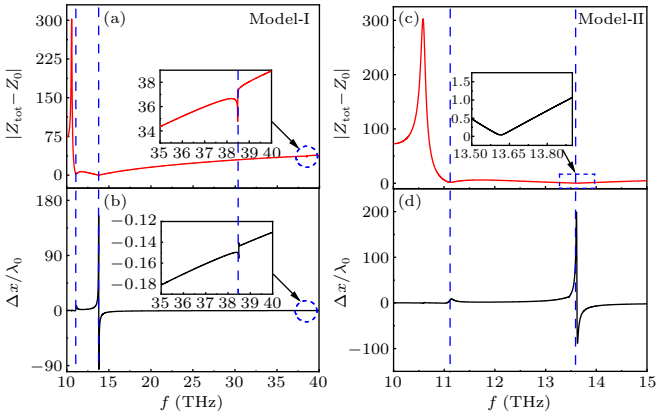


Fig. 4. Impedance of the BP–ZnS–SL structure and the GH shift versus the frequency at $N = 1$, $n_B = 1.0 \times 10^{13}$ cm^{-2}, $L_x = L_y = 100$ nm and (a) $\theta = 60.89°$ for model-I, (b) $\theta = 60.91°$ for model-II.

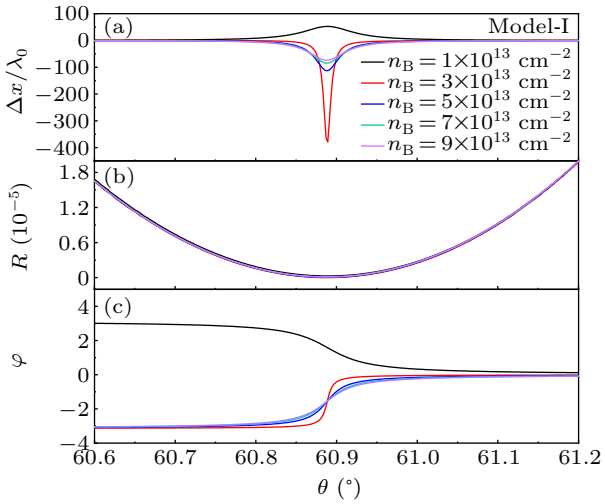


Fig. 5. Variation of (a) GH shift, (b) reflectivity and (c) phase with respect to angle of incidence under different n_B at $f = 13.74$ THz, $N = 1$ and $L_x = L_y = 100$ nm for model-I.

Next, we investigate the regulation of BP on the GH shift by varying the carrier density, layer number, and size of BP. At first, we consider the effect of n_B on the GH shift since it is easily controlled by changing the gate voltage. For model-I, the GH shift, reflectivity, and phase with respect to θ at 13.74 THz are presented in Fig. 5. With the increasing of n_B, the GH shift turns from the positive to the negative one, and a large GH shift about $\Delta x_{max} \approx -378.98\lambda_0$ is obtained at $n_B = 3 \times 10^{13}$ cm^{-2}. The lowest points of reflectivity are closer to zero and the phase becomes sharper, indicating that the incident angle is located near the Brewster angle, i.e.,

$\theta = 60.89°$. As n_B increases further, the GH shift decreases rapidly and maintains a relatively stable value about $-73.7\lambda_0$ when $n_B \geq 7 \times 10^{13}$ cm^{-2}. On the other hand, the GH shifts at $f = 11.2$ THz and 38.48 THz (see Fig. 4(b)) are very small, while it has been proven that the GH shifts are independent of n_B. For model-II, figure 6 illustrates the variation of GH shift, reflectivity, and phase with n_B at the two special frequencies (see Fig. 4(c)), respectively. For both cases, the maximum values of GH shift are obtained at $n_B = 1 \times 10^{13}$ cm^{-2} and rapidly decrease with the increasing of n_B. In Fig. 6(a), the corresponding Brewster angle is fixed at $\theta = 61.21°$. However, in Fig. 6(b), the GH shift exhibits the red shift phenomenon as n_B increases, resulting in the different Brewster angles for each curve. Moreover, the phase curve is steeper, implying that the conditions for obtaining a larger GH shift are relatively more stringent. These findings confirm the validity of regulating GH shift via gate voltage, which may provide an effective way to flexibly increase the GH shift, leading to the optimum sensitivity of the structure.

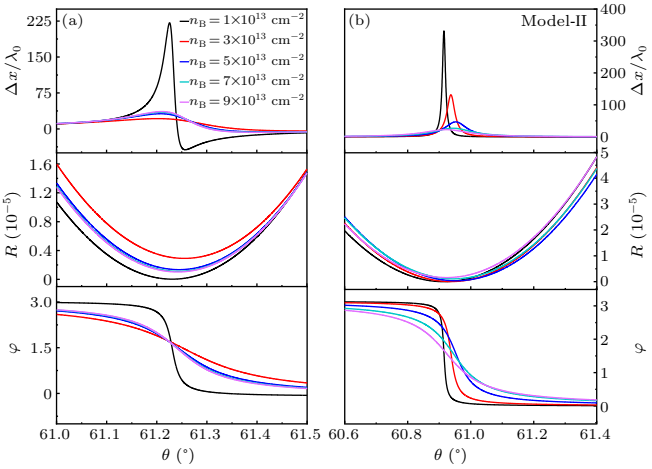


Fig. 6. Variation of GH shift, reflectivity, and phase with respect to angle of incidence under different n_B at (a) $f = 11.12$ THz, (b) $f = 13.609$ THz, $N = 1$ and $L_x = L_y = 100$ nm for model-II.

The effect of layer number N of BP film on the GH shift is investigated further, and the maximum values of GH shift are screened out by precisely adjusting the size of BP while remaining $n_B = 3 \times 10^{13}$ cm^{-2}. We limit L_x and L_y to vary from 10 nm to 500 nm. Figure 7(a) depicts the maximum GH shift caused by a blue shift at $f = 11.2$ THz if $N < 5$, resulting in different Brewster angles for each GH shift. The largest GH shift is found at $N = 3$, which is about $-7565.58\lambda_0$. It can also be seen that the size of BP required to obtain the maximum GH shift should satisfy the condition of $L_x > L_y$. In the inset of Fig. 7(a), we present the distribution of the electric field at the maximum GH shift by using Comsol Multiphysics software. The localization effect is clearly visible on the edges of the BP-patches. Figure 7(b) demonstrates that large GH shift is found at the small size of BP-patch when $f = 13.74$ THz, such as, $\Delta x_{max} = 3150.76\lambda_0$ at $L_x = 11$ nm, $L_y = 357$ nm and $N = 2$. Unlike Fig. 7(a), the Brewster angle is normally fixed at 60.889° and the length of BP satisfies $L_x < L_y$. Since $L_x \ll D$ the interaction between the BP-patches obviously disappears, as shown in the inset of Fig. 7(b). The stronger light localization only exists around each BP-patch. Finally, figure 7(c) plots the GH shift versus the incident angle at $f = 38.48$ THz. It is apparent that when $N > 2$, the GH shift becomes negative and increases with the increase of N. The largest GH shift can be obtained at $N = 5$ and the BP-patch is close to the square. Although the interaction between the adjacent BP-patches is clearly enhanced compared to Fig. 7(b), the GH shift is reduced due to the overall reduction of the optical localization. To summarize, if a large GH shift is pursued, then we should consider the optimum combination of BP-patch size and layer number given in Fig. 7(a). However, if a small BP-patch size is expected, then we have to sacrifice the GH shift and consider the recommended dimensions in Fig. 7(b).

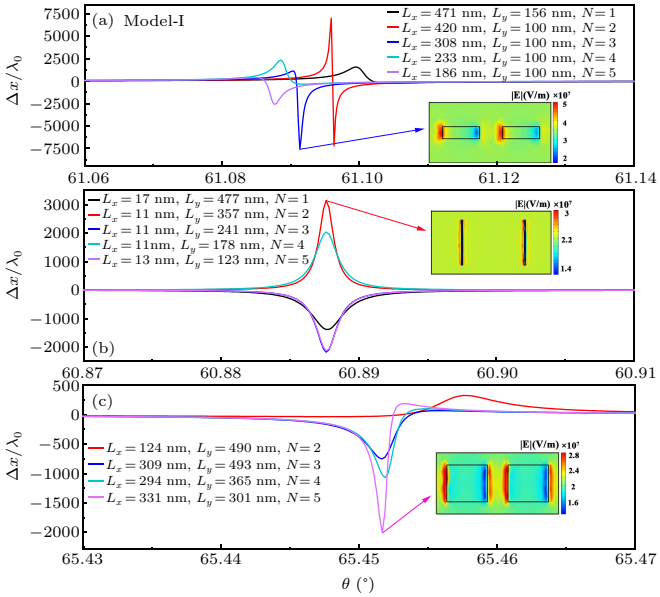


Fig. 7. Maximum of GH shift under the different size of BP and layer numbers at $n_B = 3.0 \times 10^{13}$ cm^{-2}, and (a) $f = 11.12$ THz, (b) $f = 13.609$ THz, and (c) $n_B = 1.0 \times 10^{13}$ cm^{-2}, $f = 38.48$ THz for model-I. The insets show the distributions of electric fields for the maximum GH shifts.

For model-II, according to the discussion in Fig. 6 we fix $n_B = 1 \times 10^{13}$ cm^{-2} and further adjust the size and layer number of BP to obtain the maximum of GH shift, as illustrated in Fig. 8. At $f = 11.12$ THz in Fig. 8(a), the GH shift presents a red shift phenomenon and changes from positive to negative. The maximum GH shifts achieve at $N = 1$ when $L_x = 191$ nm and $L_y = 10$ nm. The Brewster angle for each GH shift also drifts to the right as N increases. In addition, $L_x \gg L_y$ if the maximum GH shift is desired. The strength and distribution of the electric field are presented in the insets. For the case at $f = 13.609$ THz shown in Fig. 8(b), the Brewster angle is fixed at $\theta \approx 60.91°$ independent of N. In addition, when $L_x \approx L_y$ and

$N = 1$ the GH shift is largest. However, once $N > 1$, the condition $L_x > L_y$ has to be selected to obtain the maximum value of GH shift. Compared with Fig. 8(a), the maximum value of GH shift is relatively smaller, which may be understood if we carefully examine the strength of the electric field shown in the inset of Fig. 8(b). Based on the above discussion, the large GH shift can be realized by artificially designing the size and the layer number of the BP-patch in the actual device fabrication. BP is a 2D anisotropic material, which can be deposited on the surface of ZnS by the chemical vapor deposition (CVD) technique[45] and molecular beam epitaxy (MBE).[46]

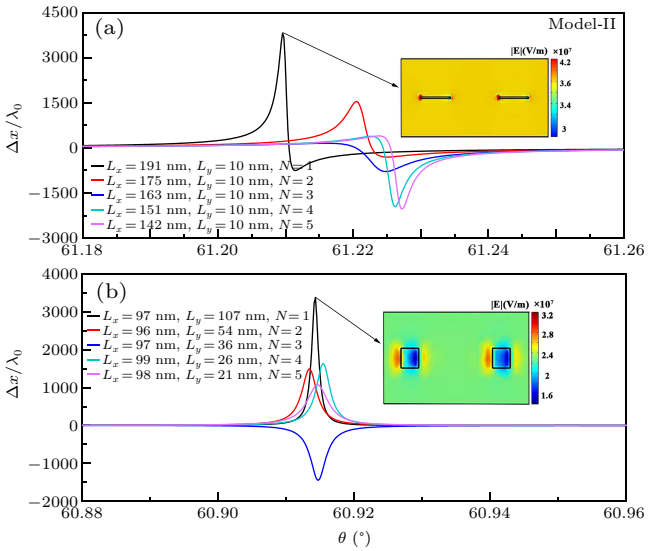


Fig. 8. Maximum of GH shift under the different size of BP and layer numbers at $n_B = 1 \times 10^{13}$ cm^{-2}, and (a) $f = 11.12$ THz and (b) $f = 13.609$ THz for model-II. The insets show the distributions of electric fields for the maximum GH shifts.

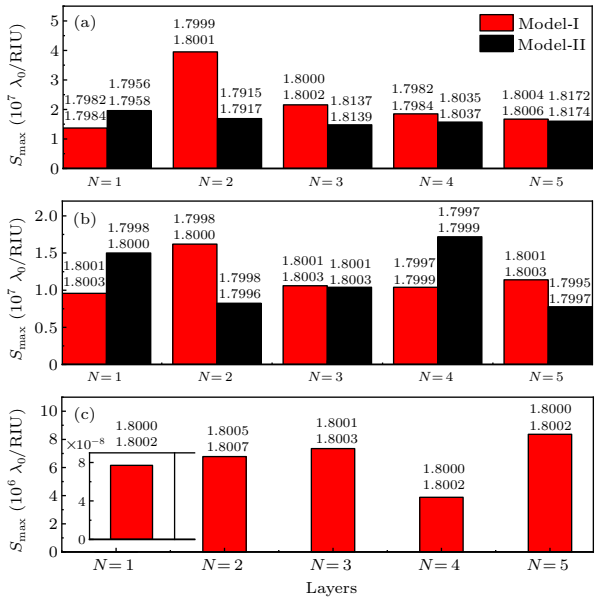


Fig. 9. Highest sensibility with the largest GH shift for the different layer numbers of BP. The refractive index varies from 1.75 RIU to 1.85 RIU. The other parameters are the same as in Figs. 7 and 8 for the different models, respectively. The inset in panel (c) shows the S is very small at $N = 1$.

Finally, based on the controllable GH shift, the possibility of its application in sensors is discussed. We use a sensitivity factor S to characterize the performance of the sensor. Both the layer number N and carrier density n_B of the BP film greatly determine the GH shift. Therefore, the control variable method is used to analyze the performance of the sensor based on GH shift under the different N and n_B at Brewster angles. The highest sensibility with largest GH shift (see Figs. 7 and 8) is sought when the refractive index varies from 1.75 RIU to 1.85 RIU with a scanning interval of 0.0002. Thus, it will make the detection of GH shift more accurate and convenient, and the sensitivity of the sensor can be improved correspondingly. The condition to produce the highest sensitivities under the different N is shown in Fig. 9, and the other parameters, including the size of the BP film, the carrier density, and the frequency, are the same as Fig. 7 for the model-I and Fig. 8 for model-II, respectively. The variation of the refraction index for each S is indicated at the top of the bars. The sensibility S corresponding to the GH shift in Figs. 7(a) and 8(a) is presented in Fig. 9(a). The maximum value of S can reach 3.95×10^7 λ_0/RIU at $N = 2$ for model-I and 1.62×10^7 λ_0/RIU at $N = 1$ for model-II. Moreover, the order of magnitude of S remains 10^7 λ_0/RIU for both models, with only a little difference when $N > 2$. Figure 9(b) presents the largest sensibility related to the GH shift in Figs. 7(b) and 8(b). It can be seen that the sensibility at $N = 2$ can reach about 1.5×10^7 λ_0/RIU for model-I and 1.72×10^7 λ_0/RIU at $N = 4$ for model-II. Compared with Fig. 9(a), the sensibility is obviously smaller. In particular, the smallest S is about 7.78×10^6 λ_0/RIU at $N = 5$ for model-II. Finally, we check the sensibility at $f = 38.48$ THz only for model-I related to Fig. 7(c). As shown in Fig. 9(c), the largest sensibility will reach 8.36×10^6 λ_0/RIU at $N = 5$, which is smaller than the largest ones obtaining for the other two frequencies by an order of magnitude. The inset gives the sensibility S for $N = 1$ although the GH shift is not shown in Fig. 7(c). It is clearly seen that the order of magnitude of the corresponding S is 10^{-7} λ_0/RIU, which may imply that a small GH shift has the potential to accompany a small sensitivity S. To summarize, it can be deduced that not only large GH shifts but also the flexible adjustment of sensibility are achieved in the BP–ZnS–SL sensor. It is noteworthy that the carrier density n_B has a great influence on GH shift, which can be easily controlled by the external field. Thus, we will consider the sensibility regulation of n_B when the proposed structure is applied to the sensor.

Based on the simulation results with N, we investigated the effect of n_B on the sensibility, as shown in Fig. 10. The physical parameters are same as those in Fig. 9, including the selection of the refraction index for each curve. In general,

the S of model-I is higher than that of model-II, which can be the order of 10^8 λ_0/RIU; for example, $S = 6.43 \times 10^8$ λ_0/RIU at $N = 5$, $n_B = 2.98 \times 10^{13}$ cm^{-2} and $f = 11.2$ THz as well as $S = 5 \times 10^8$ λ_0/RIU at $N = 4$, $n_B = 0.997 \times 10^{13}$ cm^{-2}, and $f = 38.48$ THz. It can be seen from the above discussion that the precise control of the carrier density helps to obtain the higher sensibility in BP–ZnS–SL sensor. Compared with that in the symmetrical graphene-cladding waveguide and in a graphene–hBN heterostructure,[32] the sensibility obtained in the BP–ZnS–SL metasurface structure is enhanced at least two orders of magnitude, which suggests the potential application of sensors based on the GH shift in THz range.

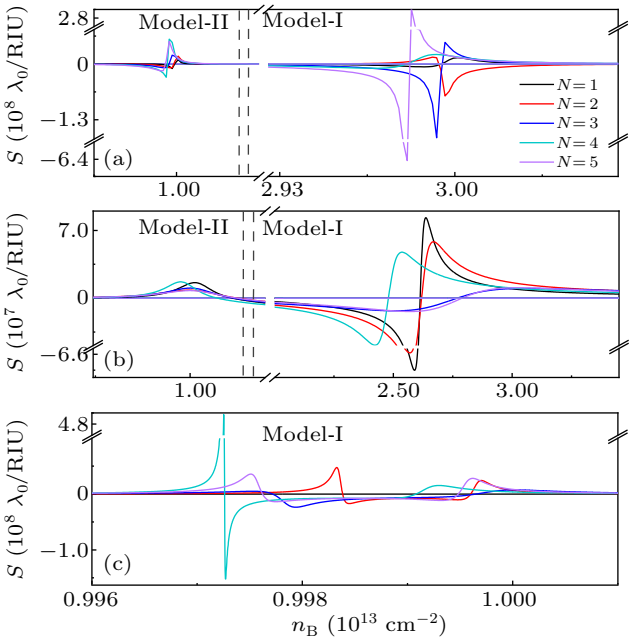


Fig. 10. Sensibility versus n_B for the different layer numbers based on Fig. 9.

4. Conclusion

In conclusion, we propose a strategy to achieve tunable and larger GH shifts with the high sensibility in THz range via the excitation of SPPPs based on the BP–ZnS–SL metasurface structure. Under different N, the largest GH shifts are predicted by dynamically adjusting the BP-patch size and the electron doping level. A comparison was made for the GH shift between model-I and model-II near the RB of ZnS and the transition of BP's conductivity. It has been demonstrated that the largest GH shift can reach about -7565.58 λ_0 at $f = 11.2$ THz and $\theta = 61.095°$ when $N = 3$, $n_B = 3 \times 10^{13}$ cm^{-2}, $L_x = 308$ nm and $L_y = 100$ nm for model-I. The localized electric field around BP-patches can enhance the GH shift significantly. As a SPPP sensor based on the changing GH shift in THz range, the sensibility can reach at 6.43×10^8 λ_0/RIU when the index refraction of the senor medium is in the range of 1.75 RIU–1.85 RIU and the scan interval is 0.0002. The sensibility is at least two orders of magnitude larger than that of the conventional SPR sensor, which is extremely sensitive to the parameters of BP, including the size, carrier density, and the layer number near Brewster angles. These findings can serve as a theoretical foundation for designing SPPP sensors with high sensibility accompanied by a large GH shift in THz frequency.

Acknowledgments

Project supported by the Natural Science Foundation of Heilongjiang Province of China (Grant No. LH2020A014) and the Graduate Students' Research Innovation Project of Harbin Normal University (Grant No. HSDSSCX2022-47).

References

[1] Goos F and Hanchen H 1947 *Ann. Phys.* **436** 333
[2] Fedorov F I 1955 *Dokl. Akad. Nauk SSSR* **105** 465
[3] Artmann K 1948 *Annalen der Physik* **437** 87
[4] Zhou X, Cheng W B, Liu S, Zhang J Q, Yang C F and Luo Z M 2021 *Opt. Commun.* **483** 126655
[5] Ling X, Zhang Z, Chen S Z, Zhou X X and Luo H L 2021 *J. Phys. D: Appl. Phys.* **55** 133001
[6] Merano M, Aiello A and Van Exter M P, Eliel E R and Woerdman J P 2007 *Opt. Express* **15** 15928
[7] Liu F, Xu J P, Song G and Yang Y P 2013 *J. Opt. Soc. Am. B* **30** 1167
[8] Ye G Z, Zhang W S, Wu W J, Chen S Z, Shu W X, Luo H L and Wen S C 2019 *Phys. Rev. A* **99** 023807
[9] Ali K, Syed A A, Waseer W I and Naqvi Q A 2021 *Optik.* **243** 167501
[10] Song H Y, Fu S F, Zhang Q, Zhou S and Wang X Z 2021 *Opt. Express* **29** 19068
[11] Li G, Luican A, Lopes dos Santos J M B, Reina A, Kong J and Andrei E Y 2010 *Nat. Phys.* **6** 109
[12] Petrov N I, Danilov V A, Popov V V and Usievich B A 2020 *Opt. Express* **28** 7552
[13] Wu F, Luo M, Wu J J, Fan C, Qi X, Jian Y R, Liu D J, Xiao S Y, Chen G Y, Jiang H T, Sun Y and Chen H 2021 *Phy. Rev. A* **104** 023518
[14] Wu F, Wu J J, Guo Z W, Jiang, H T, Sun Y, Li Y H, Ren J and Chen H 2019 *Phy. Rev. Appl.* **12** 014028
[15] Ribeiro-Palau R, Zhang C, Watanabe K, Taniguchi T, Hone A and Cory R D 2018 *Science* **361** 690
[16] Tatjana G and Ortwin H 2017 *Opt. Express* **25** 11466
[17] Engel M, Steiner M and Avouris P 2014 *Nano Lett.* **14** 6414
[18] Wang J, Jiang Y and Hu Z 2017 *Opt. Express* **25** 22149
[19] Amin M, Farhat M and Bağcı H 2013 *Opt. Express* **21** 29938
[20] Liang L, Wang J, Lin W L, Sumpter B G, Meunier V and Pan M H 2014 *Nano Lett.* **14** 6400
[21] Yuan H T, Liu X G, Afshinmanesh F, Li W, Xu G, Sun J, Lian B, Alberto G. Curto, Ye G J, Hikita Y, Shen Z X, Zhang S C, Chen X H, Brongersma M, Harold Y H and Cui Y 2015 *Nat. Nanotechnol.* **10** 707
[22] Li Y B, Song H Y, Zhang Y Q, Zhou S, Fu S F, Zhang Q and Wang X Z 2023 *Opt. Laser Technol.* **159** 108968
[23] Zhang W S, Wang Y S, Chen S Z, Wen S C and Luo H L 2022 *Phys. Rev. A* **105** 043507
[24] Guo T, Jin B and Argyropoulos C 2019 *Phys. Rev. Appl.* **11** 024050
[25] Mitra S S and Massa N E 1982 *Band Theory and Transport Properties* (Vol. I) (North-Holland) pp: 81–192
[26] Caldwell J D, Lindsay L, Giannini V, Vurgaftman I, Reinecke T L, Maier S A and Glembocki O J 2015 *Nanophotonics* **4** 44
[27] Wang T, Li P, Hauer B, Chigrin D N and Taubner T 2013 *Nano Lett.* **13** 5051
[28] Lin Z, Jiang L, Wu L, Guo J, Dai X, Xiang Y and Fan D 2016 *IEEE Photonics J.* **8** 1
[29] Pourhassan H, Safari E, Reza T M and Aghanejad A 2022 *Opt. Laser Technol.* **148** 107756
[30] Li Z, Zhang Y, Guo X W, Tong C H, Chen X Y, Zeng Y, Shen J and Li C Y 2023 *Opt. Express* **31** 3520
[31] You Q, Shan Y, Gan S W, Zhao Y T, Dai X Y and Xiang Y J 2018 *Opt. Mater. Express* **8** 3036

[32] Liu Z, Lu F, Jiang L, Lin Y and Zhang Z W 2021 *Biosensors* **11** 201
[33] Zhou X, Liu S, Ding Y, Li M and Luo Z M 2019 *Carbon* **149** 604
[34] Wu S Q, Song H Y, Li Y B, Fu S F and Wang X Z 2022 *Results Phys.* **35** 105383
[35] Kumar A, Low T, Fung K H, Avouris P and Fang N X 2015 *Nano Lett.* **15** 3172
[36] Nemilentsau A, Low T and Hanson G 2016 *Phys. Rev. Lett.* **116** 066804
[37] Gan C H 2012 *Appl. Phys. Lett.* **101** 111609
[38] Zhang Q, Zhou S, Fu S F and Wang X Z 2019 *J. Opt. Soc. Am. B* **36** 1429
[39] Guo T and Argyropoulos C 2019 *J. Opt. Soc. Am. B* **36** 2962
[40] Ramaccia D, Toscano A and Bilotti F 2011 *Prog. Electromagn. Res. M* **21** 1
[41] Mishra V, Costa F and Monorchio A 2020 *IEEE International Symposium on Antennas and Propagation and North American Radio Science Meeting* 903–904
[42] Zheng Z, Lu F, Jiang L, Jin X L, Dai X Y and Xiang Y J 2019 *Opt. Commun.* **452** 227
[43] Mitra S S and Massa N E 1982 *Handbook on Semiconductors* (Ch. 3) (North-Holland: Paul W, Amsterdam)
[44] Zhang W., Wu W J, Chen S Z, Zhang J, Ling X H, Shu W X, Luo H L and Wen S C 2018 *Photon. Res.* **6** 511
[45] Smith J B, Hagaman D and Ji H F 2016 *Nanotechnology* **27** 215602
[46] Hu Z H, Niu T C, Guo R, Zhang J L, Lai M, He J, Wang L and Chen W 2018 *Nanoscale* **10** 21575